

Manuscript Number: SMM-19-46R1

Title: Growth of  $\beta$  intermetallic in Al-Cu-Si alloy during directional solidification via machine learned 4D quantification

Article Type: Regular article

Keywords: Al alloys, Intermetallics, 4D Imaging, Machine learning

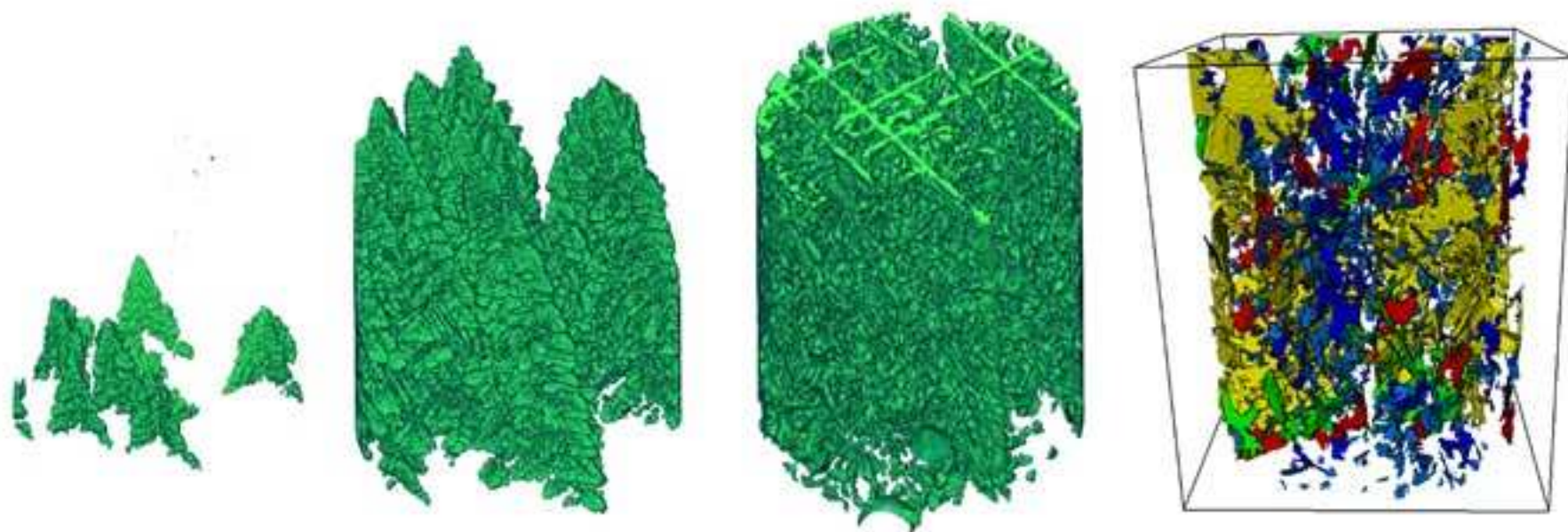
Corresponding Author: Dr. Biao Cai,

Corresponding Author's Institution: Univerisity of Manchester

First Author: Biao Cai

Order of Authors: Biao Cai; Andrew Kao; Peter D Lee; E Boller; H Basevi; A. B Phillion; A Leonardis; K Pericieous

Abstract: Fe contamination is a serious composition barrier for Al recycling. In Fe-containing Al-Si-Cu alloy, a brittle and plate-shaped  $\beta$  phase forms, degrading the mechanical properties. 4D (3D plus time) synchrotron X-ray tomography was used to observe the directional solidification of Fe-containing Al-Si-Cu alloy. The quantification of the coupled growth of the primary and  $\beta$  phase ( $Al_5FeSi$ ) via machine learning and particle tracking, demonstrates that the final size of the  $\beta$  intermetallics were strongly influenced by the solute segregation and space available for growth. The temperature gradient direction controlled the  $\beta$  orientation. The work can be used to validate predictive models.



**Primary phase**

**$\beta$  intermetallics**

**Supplementary Material Movie 1**

[Click here to download Supplementary Material: SM1.avi](#)

**Supplementary Material Movie 2**

[Click here to download Supplementary Material: SM2.avi](#)

**Supplementary Material Movie 3**

[Click here to download Supplementary Material: SM3.avi](#)

1                    **Growth of  $\beta$  intermetallic in an Al-Cu-Si alloy during directional**  
2  
3                    **solidification via machine learned 4D quantification**

4  
5                    B.Cai<sup>a,\*</sup>, A. Kao<sup>b</sup>, P.D. Lee<sup>c, \*\*</sup>, E. Boller<sup>d</sup>, H. Basevi<sup>e</sup>, A. B. Phillion<sup>f</sup>, A.

6  
7  
8                    Leonardis<sup>e</sup>, K. Pericieous<sup>b</sup>

9  
10  
11                    <sup>a</sup> *School of Metallurgy and Materials, University of Birmingham, UK;*

12  
13                    <sup>b</sup> *Centre for Numerical Modelling and Process Analysis, University of Greenwich, UK;*

14  
15                    <sup>c</sup> *School of Mechanical Engineering, University College London, UK;*

16  
17                    <sup>d</sup> *ESRF-The European Synchrotron, 71 Avenue des Martyrs, 38000 Grenoble, France;*

18  
19                    <sup>e</sup> *School of Computer Science, University of Birmingham, UK;*

20  
21                    <sup>f</sup> *Dept. of Materials Science and Engineering, McMaster University, Hamilton, Canada*

22  
23  
24  
25  
26  
27  
28  
29  
30  
31                    **\*b.cai@bham.ac.uk**  
32  
33  
34  
35  
36  
37  
38  
39  
40  
41  
42  
43  
44  
45  
46  
47  
48  
49  
50  
51  
52  
53  
54  
55  
56  
57  
58  
59  
60  
61  
62  
63  
64  
65

# Growth of $\beta$ intermetallic in an Al-Si-Cu alloy during directional solidification via machine learned 4D quantification

Fe contamination is a serious composition barrier for Al recycling. In Fe-containing Al-Si-Cu alloy, a brittle and plate-shaped  $\beta$  phase forms, degrading the mechanical properties. 4D (3D plus time) synchrotron X-ray tomography was used to observe the directional solidification of Fe-containing Al-Si-Cu alloy. The quantification of the coupled growth of the primary and  $\beta$  ( $\text{Al}_5\text{FeSi}$ ) phase via machine learning and particle tracking, demonstrates that the final size of the  $\beta$  intermetallics were strongly influenced by the solute segregation and space available for growth whereas the  $\beta$  orientation was controlled by the temperature gradient direction. The work can be used to validate predictive models.

Keywords: Al alloys, Intermetallics, Synchrotron X-ray Tomography, 4D Imaging

The full life cycle of aluminium is attractive because recycled aluminium requires as little as 5% of the energy needed for primary production, hence reducing greenhouse emissions [1,2]. However, iron (Fe) continuously accumulates during repeated recycling [3]. As it has low solid solubility in Al, the formation of Fe-rich intermetallic particles during solidification/casting is normally unavoidable [4]. For example, in Al-Si based alloys which have been widely used in engine blocks for automobiles, with the addition of Fe,  $\beta$  phase ( $\text{Al}_5\text{FeSi}$ ) can normally form [5–8]. The  $\beta$  phase is plate-shaped and brittle, thereby detrimental to the mechanical properties of the final products[8]. Understanding the nucleation and growth mechanisms of  $\beta$  phase has attracted significant research interest as this knowledge can facilitate the development of innovative and crucially-needed methods to alleviate its unfavourable effects [2]. Solidification of Fe-containing Al alloys has been studied using *in situ* X-ray imaging, providing information on the nucleation and morphological evolution of Fe-containing intermetallics [7,9–14]. Terzi *et al* [10] observed the nucleation of the  $\beta$  phase on the oxide skins and the subsequent growth of the  $\beta$  phase into complex shapes using high

1 speed X-ray tomography. Puncreobutr *et al* [7] performed a similar experiment with  
2 higher temporal resolution. They observed that the nucleation of the  $\beta$  phase was mainly  
3 on or near the primary Al dendrites. Additionally, the growth of the  $\beta$  phase is found to  
4 be significantly influenced by the primary dendrite arms [7]. Recently, the influence of  
5 strontium addition and cooling rates on the intermetallic evolution in Fe-containing Al-  
6 10Si alloys was studied by Yu *et al* [11], demonstrating that change of thermal  
7 processing conditions and alloy composition could impact the Fe-containing particles.  
8 However, none of those studies controlled the thermal field direction; therefore, the  
9 growth of intermetallics with regard to the temperature field has not been clearly  
10 demonstrated. Moreover, there is litter knowledge regarding to the coupled growth of  
11 the primary phase and the intermetallics.

12 In this study, we aim to illustrate the evolution of  $\beta$  intermetallics during directional  
13 solidification of an Al-Si-Cu alloy. High-speed synchrotron X-ray tomography was used  
14 to capture the solidification sequence. Detailed quantification of both the primary  
15 dendrite and  $\beta$  phase was carried out, providing new insights into the coupled growth of  
16 the two phases under a directional temperature field. This result can be used to develop  
17 and validate analytical and numerical models for the coupled crystal growth.

18 The Al-Si-Cu W319 alloy (Al-5.50Si-3.40Cu-0.87Fe-0.27Mg, weight percent) used in  
19 this study was provided by Ford Motor Company. A cylinder sample of diameter 1.8  
20 mm was machined by wire-electrical discharge machining. The temperature gradient  
21 stage was set up at ID19, European Synchrotron Radiation Facility. The details about  
22 the temperature gradient stage, similar to the one in Ref [15] are provided in the  
23 supplementary material

24 A pink beam with peak energy at 35 keV was used at ID19, ESRF. A high-speed  
25 CMOS camera (PCO.DIMAX, Germany) was used for X-ray imaging. The field of

1 view (FOV) of the camera was set to 2.2 by 2.2 mm and the pixel size is 2.2  $\mu\text{m}$ . The  
2 sample was rotated at 2 s per rotation for tomographic data collection. A tomogram with  
3 1000 projections over 180  $^\circ$  was taken in 1 s and there were 15 s waiting time between  
4 two consecutive tomograms for data downloading.  
5  
6

7  
8  
9 The 319 Al sample was heated up until it was fully molten with a temperature gradient  
10 of  $\sim 10$   $^\circ\text{C}/\text{mm}$  between the two furnaces (the top furnace was hotter). As the  
11 thermocouples were attached to the furnaces, and further away from the sample, the  
12 measured temperature was different from the sample temperature. After the sample in  
13 the FOV was fully molten, it was held for 15 min. After that, both furnaces were cooled  
14 down at the same cooling rate of 0.1  $^\circ\text{C}/\text{s}$ , which allows the directional growth of the  
15 primary phase. As the sample started cooling, high-speed X-ray tomography was  
16 started. 47 tomograms were collected and reconstructed by ESRF's reconstruction  
17 algorithm with phase retrieval.  
18  
19  
20  
21  
22  
23  
24  
25  
26  
27  
28  
29  
30

31 Figs. 1a-1f show the vertical cross-section slice at the central plane of the sample as a  
32 function of time (supplementary movie S1). The primary phase is dark grey while the  
33 liquid is light grey.  $t_0$  is denoted as the time at which the primary phase first appeared in  
34 the FOV. The primary phase is observed growing upwards from the bottom of the FOV  
35 with a dendritic structure. At  $t = t_0 + 224$  s, bright needle-like structures appear within  
36 the liquid channels between dendrites (some marked by the arrows in Fig. 1e). These  
37 were identified as  $\beta$  intermetallics due to two reasons: (i) they were plate shaped,  
38 similar to [7]; and (ii) based on the solidification sequence of W319 alloy (see the  
39 supplementary material), the phase formed after the primary phase should be the  $\beta$   
40 intermetallic. Because of its higher Fe content than the melt, it appears much brighter  
41 than both the melt and the primary phase in the tomographic slices (e.g. Fig.1e).  
42  
43  
44  
45  
46  
47  
48  
49  
50  
51  
52  
53  
54  
55  
56  
57  
58  
59  
60  
61  
62  
63  
64  
65

1 With Scheil solidification calculation, the temperature gradient and cooling rate of the  
2 sample were then estimated (See the supplement for the procedure). The temperature  
3  
4 gradient was estimated to be 6.4 °C/mm and the cooling rate was around 0.078 °C/s,  
5  
6 both of which were smaller than the values measured by the thermocouples away from  
7  
8 the sample.  
9  
10

11 We then used Avizo 9.4 (ThermoFisher Scientific) to analyse the 3D images. For the  
12  
13 primary phase, a 3D anisotropy diffusion filter followed by an interactive threshold was  
14  
15 used. The segmented dendritic structure is shown in Figs.1g-1l and in the  
16  
17 supplementary movie S2. Six primary dendrites grew from the bottom of the sample  
18  
19 initially, merged into 4 at the later stage of solidification. The dendrites preferred to  
20  
21 grow up first at one side of the sample, indicating that macro-segregation of solutes was  
22  
23 formed on the other side, inhibiting the growth of primary phase. This indicates that  
24  
25 there might be a small horizontal temperature gradient.  
26  
27  
28  
29  
30

31 Applying a similar procedure to segment the intermetallics turned out to be difficult. To  
32  
33 resolve this issue, a machine learning based image processing plugin in ImageJ  
34  
35 (Trainable Weka Segmentation [16]) was used. The plugin combines a collection of  
36  
37 machine learning algorithms to perform pixel-based segmentations. The detailed  
38  
39 procedure for the machine learned segmentation is provided in the supplementary  
40  
41 material. This process is fully automated and could be much more timesaving compared  
42  
43 to the manual segmentation performed by Puncreobutr *et al* [7].  
44  
45  
46  
47

48 The 3D shape of the segmented intermetallic is shown in Fig. 2a to 2d (also see the  
49  
50 supplementary video S3). The intermetallics started to form from the bottom of the  
51  
52 FOV at  $t_0+208$  s, and grew upwards. Although macro-segregation was observed (Fig.  
53  
54 1h) so that the interface between the primary phase and the liquid was tilted, the  $\beta$  phase  
55  
56 grew up with a flat interface indicating that its growth was not largely affected by the  
57  
58  
59  
60  
61  
62  
63  
64  
65

1 macro-segregation. Another observation is that the intermetallics nucleated from both  
2 the sample surface and interior, consistent with Ref. [7].  
3

4 With the segmented primary and  $\beta$  phase, quantification can then be performed. The  
5 volume fraction of the primary phase during solidification is shown in Fig. 3a. It  
6 increased linearly at a rate of  $0.0016 \text{ s}^{-1}$  until it reached around 0.41 at  $t=t_0+240 \text{ s}$ . The  
7 dendrite growth velocity was measured via tracking the tip position of the dendrite  
8 primary arms during solidification. The velocity of four dendrites out of six are shown  
9 in Fig. 3b, which have a similar trend. The velocity was highest at the early stage of  
10 solidification ( $\sim 24 \text{ }\mu\text{m/s}$  at  $t_0+32 \text{ s}$ ), then slowed down to be at around  $8 \text{ }\mu\text{m/s}$  from  
11  $t_0+80 \text{ s}$  onwards. It is not possible to measure the velocity after the tip reached the top of  
12 the FOV at  $t= t_0+128 \text{ s}$ .  
13  
14  
15  
16  
17  
18  
19  
20  
21  
22  
23  
24  
25  
26

27 Fig. 3a shows the volume fraction of  $\beta$  versus time. The  $\beta$  volume fraction increased  
28 almost linearly at a rate of  $9.5 \times 10^{-5} \text{ s}^{-1}$ . The total number of the  $\beta$  intermetallic and its  
29 average volume (total volume of  $\beta$ /total number) against time is shown in Fig. 3c. The  
30 total number increased continuously in a linear fashion, as did the average volume. At  
31 the end of the experiment ( $t_0+464 \text{ s}$ ), 989 intermetallics are found within the FOV. We  
32 then measured the volume fraction of intermetallic particles at different heights of the  
33 sample. Volumetric data with 30 slices at each chosen height were used for the  
34 measurement. As shown in Fig.3d, the curves ( $\beta$  volume fraction as a function of time  
35 ( $t$ ) at different heights ( $h$ )) were almost linear with very similar slopes. The intercept of  
36 these curves with the x-axis corresponded to the time ( $t_0$ ) at which  $\beta$  phase just  
37 appeared at the chosen height. The  $t_0$  at different heights of the sample is then plotted  
38 in Fig.3e. A slope of about  $11.7 \text{ }\mu\text{m/s}$  was obtained after a linear fitting, which means  
39 that the isotherm moved upwards at a speed of  $11.7 \text{ }\mu\text{m/s}$  as the sample was cooling  
40 down. The speed of the isotherm can also be calculated by the ratio of the cooling rate  
41  
42  
43  
44  
45  
46  
47  
48  
49  
50  
51  
52  
53  
54  
55  
56  
57  
58  
59  
60  
61  
62  
63  
64  
65

1 to the temperature gradient, resulting in a very close value of  $\sim 12.2 \mu\text{m/s}$ . This indicates  
2 that our temperature estimation was relatively accurate.  
3

4 As the sample was cooled down at a constant cooling rate, a linear function between the  
5 temperature ( $T(h)$ ) at the sample height ( $h$ ) and the processing time ( $t$ ) can be  
6 established by Eq. 1:  
7  
8  
9  
10

$$(1)$$

11 where  $T_{\beta}$  is the  $\beta$  occurrence temperature ( $595 \text{ }^{\circ}\text{C}$ ),  $R$  is the cooling rate ( $0.078 \text{ }^{\circ}\text{C/s}$ ).  
12

13 Fig.3d can then be re-plotted to  $\beta$  volume fraction versus temperature via eq. 1 (Fig. 3f)  
14 along with the Scheil predictions. The experimental result matches well with the Scheil  
15 simulation at the early stage of  $\beta$  formation ( $595$  to around  $582 \text{ }^{\circ}\text{C}$ ). However, the  
16 prediction and experimental result differ from each other at the later stage of  
17 solidification. Similar difference is also reported in [7]. This indicates that although the  
18 Scheil model based on equilibrium can predict well the nucleation stage of the  
19 intermetallic, it could not make good prediction for the growth stage.  
20  
21  
22  
23  
24  
25  
26  
27  
28  
29  
30  
31  
32  
33

34 The overall behaviour of  $\beta$  phase with respect to the average volume, total number and  
35 volume fraction was linear with decreasing temperature. However, the behaviour of  
36 individual  $\beta$  intermetallics remained unclear. To examine this, a particle-tracking  
37 algorithm was developed in-house in Matlab (see supplementary material). The volume  
38 change ( $\frac{dV}{dt}$ ,  $V$  is the volume) of several individual particles which  
39 first appeared at  $t = t_0 + 240 \text{ s}$  is shown in Fig. 4a. The growth dynamics of the  
40 intermetallics varied significantly, but most of them grow linearly. We then fitted the  
41 curves of the tracked particles' volume vs time with linear functions. The slopes are the  
42 volume growth rate of the  $\beta$  intermetallics. Fig. 4b shows the histogram of the volume  
43 growth rate of the intermetallics on a log x-axis, which shows a normal distribution. The  
44 intermetallics were then separated and coloured based on the volume growth rate as  
45  
46  
47  
48  
49  
50  
51  
52  
53  
54  
55  
56  
57  
58  
59  
60  
61  
62  
63  
64  
65

1 shown in Fig. 4c (green – intermetallics with velocity less than 7, 000  $\mu\text{m}^3/\text{s}$  whereas  
2 purple – more than 7, 000  $\mu\text{m}^3/\text{s}$ ). 7, 000  $\mu\text{m}^3/\text{s}$  was chosen based on the histogram (Fig.  
3  
4 4b). The particles with higher velocity have the following characteristics: (1) connected  
5  
6 to the sample outer surface (Fig. 4c); (2) located within the regions where macro-  
7  
8 segregation was observed and/or within primary dendrite arms (Fig. 4d); and (3) they  
9  
10 were connected particles (several particles grew together into a single one). The  
11  
12 particles with smaller volume growth rates distributed more homogeneously across the  
13  
14 sample (Fig. 4c) and the majority of the particles with a lower growth rate were located  
15  
16 within the sample interior. A closer look at those particles shows that they were mostly  
17  
18 within secondary dendrite arms (Fig. 4e). The variation of the growth velocity indicates  
19  
20 that the growth of  $\beta$  particles was influenced by the local environment they experienced  
21  
22 (e.g. composition variation due to micro and macro segregation, and the space available  
23  
24 for growth). If an  $\beta$  intermetallic nucleated in the region with macro-segregation, it had  
25  
26 abundant solutes and liquid space for growth hence it grew large. If the  $\beta$  phase  
27  
28 nucleated in the region within the secondary dendrite arms, its growth would be much  
29  
30 more restricted. This finding can have implications for modelling intermetallic growth  
31  
32 in casted components [17,18] – the size and growth rate of the intermetallics are directly  
33  
34 related to the macro segregation behaviour of the casted components.  
35  
36  
37  
38  
39  
40  
41  
42

43 We then used an ImageJ plugin-BoneJ [19] to measure the local thickness of the  
44  
45 intermetallics, defined as the diameter of the greatest sphere that can fit within the  
46  
47 structure. The 3D rendering of the local thickness is shown in Fig. 2e and 2f. Fig. 4d  
48  
49 shows the mean local thickness and its standard deviation against time. It increased  
50  
51 from 8 to only 11  $\mu\text{m}$  during solidification. The mean local thickness at  $t=t_0+464$  s is 11  
52  
53  $\mu\text{m}$  with a standard deviation of 4  $\mu\text{m}$ . The maximum is about 20  $\mu\text{m}$ . The reluctant  
54  
55 increase of local thickness was also observed by [7].  
56  
57  
58  
59  
60  
61  
62  
63  
64  
65

1 To determine the orientation of those particles, we used principal component analysis  
2 (PCA) as described in [7,20]. Assuming the  $\beta$  phase was plate-shaped, the 3<sup>rd</sup>  
3 component of PCA analysis shall be the normal direction of the plates. The angle ( $\theta$ )  
4 between the 3<sup>rd</sup> component and the vertical direction (Z) of the tomographic volume  
5 should determine the orientation of the intermetallics with respect to the temperature  
6 field direction (Z). However, for intermetallics complicated in geometry with holes and  
7 branches and/or connected with others (Fig.4e),  $\theta$  value derived from PCA may not  
8 correctly measure their orientations. To remove those particles from the  $\theta$  calculation,  
9 an empirical method was applied - particles with plate thickness (module of the 3<sup>rd</sup> PCA  
10 component) larger than 20  $\mu\text{m}$  were not used for the orientation calculation. This value  
11 was chosen according to the BoneJ measurement that the maximum local thickness was  
12  $\sim 20 \mu\text{m}$ . Fig. 4h shows the polar histogram of the angle  $\theta$  at two time steps. The  $\theta$  angle  
13 was distributed mainly within 60 to 120°, and peaked at around 90°. This shows that  
14 most of the  $\beta$  phase was oriented almost parallel to the Z direction, which indicates that  
15 the growth direction of the  $\beta$  phase was strongly influenced by the heat flow induced by  
16 the directional temperature gradient.  
17  
18  
19  
20  
21  
22  
23  
24  
25  
26  
27  
28  
29  
30  
31  
32  
33  
34  
35  
36  
37  
38

39 In summary, 4D synchrotron X-ray tomography was used to study directional  
40 solidification of a Fe-containing W319 Al alloy. The work shows that the overall  
41 growth of the primary and  $\beta$  phase was linear as a function of time/temperature when  
42 the sample was cooling down at a constant cooling rate of 0.078 °C/s under a  
43 temperature gradient of 6.4 °C/mm. During solidification, a macro-segregation zone  
44 formed on one side of the sample. The growth rate of the  $\beta$  intermetallics were largely  
45 determined by the interdendritic space available for growth. The intermetallics  
46 nucleated in the macro-segregation zone as well as some large inter-primary dendritic  
47 liquid regions had abundant space to grow hence grew quickly to large crystals. The  
48  
49  
50  
51  
52  
53  
54  
55  
56  
57  
58  
59  
60  
61  
62  
63  
64  
65

1 intermetallics nucleated between the secondary dendrite arms were restricted and grew  
2 slower. The heat flow direction influenced the orientation of  $\beta$  intermetallics, so that the  
3 normal vector of the plate-shape intermetallics was perpendicular to the heat flow  
4 direction.  
5  
6  
7  
8  
9

## 10 **Acknowledgement**

11 This work was supported the EPSRC-UK (EP/I02249X/1 and EP/K007734/1). The  
12 authors thank the European Synchrotron Radiation Facility for providing the beamtime  
13 (MA2989) and staff at ID19 beamline for support. B.C. acknowledges the support from  
14 the Diamond Birmingham Collaboration and the Alan Turing Fellowship.  
15  
16  
17  
18  
19  
20  
21  
22  
23

## 24 **References**

- 25  
26  
27 [1] John A. S. Green, Aluminum Recycling and Processing, ASM International, 2007.  
28  
29 [2] C.B. Basak, N.H. Babu, Sci. Rep. 7 (2017) 1–10.  
30 [3] L. Zhang, J. Gao, L.N.W. Damoah, D.G. Robertson, Miner. Process. Extr.  
31 Metall. Rev. 33 (2012) 99–157.  
32 [4] T.O. Mbuya, B.O. Odera, S.P. Ng'ang'a, Int. J. Cast Met. Res. 16 (2003) 451–  
33 465.  
34 [5] T. Smith, K. O'Reilly, S. Kumar, I. Stone, Metall. Mater. Trans. A Phys. Metall.  
35 Mater. Sci. 44 (2013) 4866–4871.  
36 [6] C.B. Basak, N. Hari Babu, Mater. Des. 108 (2016) 277–288.  
37 [7] C. Puncreobutr, A.B. Phillion, J.L. Fife, P. Rockett, A.P. Horsfield, P.D. Lee,  
38 Acta Mater. 79 (2014) 292–303.  
39 [8] L.A. Narayanan, F.H. Samuel, J.E. Gruzleski, Met. Mat. Trans. A 25 (1994)  
40 1761–1773.  
41 [9] J. Wang, P.D. Lee, R.W. Hamilton, M. Li, J. Allison, Scr. Mater. 60 (2009) 516–  
42 519.  
43 [10] S. Terzi, J.A. Taylor, Y.H. Cho, L. Salvo, M. Suéry, E. Boller, A.K. Dahle, Acta  
44 Mater. 58 (2010) 5370–5380.  
45 [11] J.M. Yu, N. Wanderka, A. Rack, R. Daudin, E. Boller, H. Markötter, A.  
46 Manzoni, F. Vogel, T. Arlt, I. Manke, J. Banhart, J. Alloys Compd. 766 (2018)  
47 818–827.  
48 [12] B. Kim, S. Lee, S. Lee, H. Yasuda, Mater. Trans. 53 (2012) 374–379.  
49 [13] S. Feng, E. Liotti, A. Lui, S. Kumar, A. Mahadevegowda, K.A.Q.O. Reilly, P.S.  
50 Grant, Scr. Mater. 149 (2018) 44–48.  
51 [14] A. Bjurenstedt, D. Casari, S. Seifeddine, R.H. Mathiesen, A.K. Dahle, Acta  
52 Mater. 130 (2017) 1–9.  
53 [15] B. Cai, J. Wang, A. Kao, K. Pericleous, A.B. Phillion, R.C. Atwood, P.D. Lee,  
54 Acta Mater. 117 (2016) 160–169.  
55  
56  
57  
58  
59  
60  
61  
62  
63  
64  
65

- 1 [16] I. Arganda-Carreras, V. Kaynig, C. Rueden, K.W. Eliceiri, J. Schindelin, A.  
2 Cardona, H.S. Seung, *Bioinformatics* 33 (2017) 2424–2426.  
3 [17] J. Wang, M. Li, J. Allison, P.D. Lee, *J. Appl. Phys.* 107 (2010) 1–8.  
4 [18] J. Allison, M. Li, C. Wolverton, X.M. Su, *Jom* 58 (2006) 28–35.  
5 [19] M. Doube, M.M. Kłosowski, I. Arganda-Carreras, F.P. Cordelières, R.P.  
6 Dougherty, J.S. Jackson, B. Schmid, J.R. Hutchinson, S.J. Shefelbine, *Bone* 47  
7 (2010) 1076–1079.  
8 [20] S. Yue, P.D. Lee, G. Poologasundarampillai, J.R. Jones, *Acta Biomater.* 7 (2011)  
9 2637–2643.  
10  
11  
12  
13  
14  
15  
16  
17  
18  
19  
20  
21  
22  
23  
24  
25  
26  
27  
28  
29  
30  
31  
32  
33  
34  
35  
36  
37  
38  
39  
40  
41  
42  
43  
44  
45  
46  
47  
48  
49  
50  
51  
52  
53  
54  
55  
56  
57  
58  
59  
60  
61  
62  
63  
64  
65

1 Fig 1. (a to e) 2D longitudinal cross-sectioned slices, and (f to j) 3D rendering of the  
2 segmented primary phase: (a) and (f) at  $t_0$ ; (b) and (g) at  $t_0+36$  s; (c) and (h) at  $t_0+80$  s;  
3 (d) and (i) at  $t_0+160$  s; (e) and (j) at  $t_0+464$  s (scale bar: 300  $\mu\text{m}$ ).  
4  
5  
6

7 Fig 2. (a) An original greyscale slice at the height of 440  $\mu\text{m}$  at  $t_0+464$  s; (b) red colour  
8 showing regions segmented for the  $\beta$  phase via the interactive method; (c) probability  
9 map of the  $\beta$  after wika trainable segmentation; (d) the segmented  $\beta$  intermetallics  
10 (black needles); (e) and (f) the enlarged view of the original greyscale slice and the  
11 corresponding segmented  $\beta$  phase (black needles in the image) (scale bar: 300  $\mu\text{m}$ ).  
12  
13  
14  
15  
16

17 Fig 3. (a) to (d) volume rendering of  $\beta$  intermetallics, at  $t_0+$  (a) 224 s; (b) 288 s; (c) 352  
18 s; and (d) 464 s; (e) and (f) the distribution of local thickness of the  $\beta$  intermetallics at  
19  $t_0+$ (e) 352 s; and (f) 464 s. (scale bar: 300  $\mu\text{m}$ ).  
20  
21  
22  
23

24 Fig 4. Quantification of individual  $\beta$  intermetallics: (a) the volume change of particles  
25 appearing from  $t=t_0+240$  s; (b) the histogram of the volume velocity of  $\beta$  particles on a  
26 log x-axis; (c)  $\beta$  particles in 3D at  $t=t_0+464$  s color-coded by their velocity (low  
27 velocity - green  $< 7000$   $\mu\text{m}^3/\text{s}$ , high velocity - purple  $> 7000$   $\mu\text{m}^3/\text{s}$ ); (d)  $\beta$  particles  
28 (purple) with high velocity at  $t=t_0+464$  s and the primary phase (blue) at  $t=t_0+128$  s;  
29 (e) a region of interests showing  $\beta$  particles with low velocity (green) and primary  
30 phase (blue) at  $t=t_0+464$  s; (f) the average local thickness vs time; (g) a connected  $\beta$   
31 particle; and (h) rose histogram of angle  $\theta$ .  
32  
33  
34  
35  
36  
37  
38  
39  
40  
41  
42  
43  
44  
45  
46  
47  
48  
49  
50  
51  
52  
53  
54  
55  
56  
57  
58  
59  
60  
61  
62  
63  
64  
65

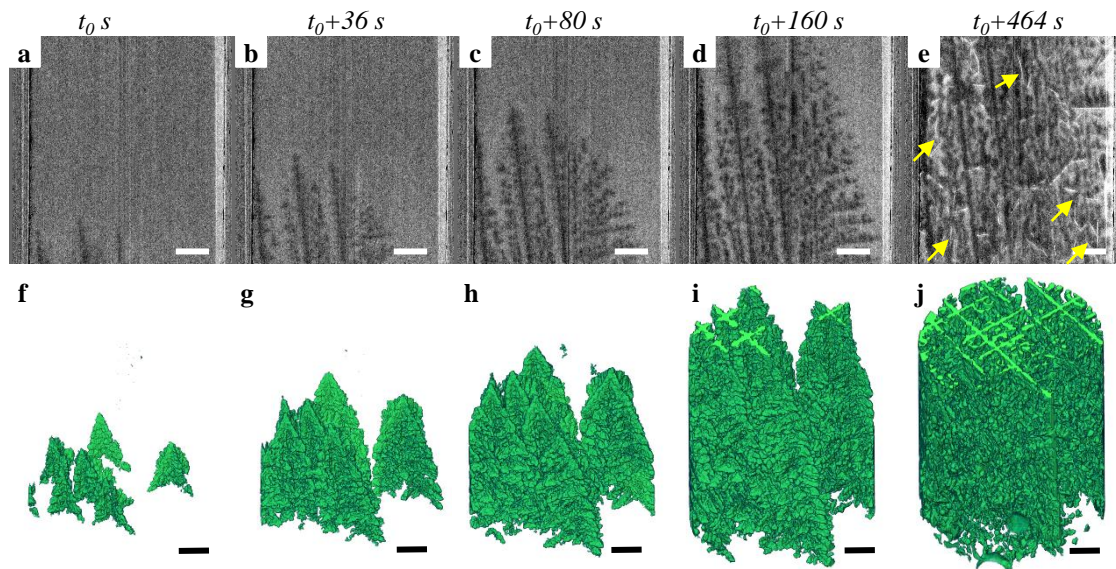


Fig.1. (a to e) 2D longitudinal cross-sectioned slices from the 4D tomography, and (f to j) 3D rendering of the segmented dendritic primary phase: (a) and (f) at  $t_0$ ; (b) and (g) at  $t_0+36$  s; (c) and (h) at  $t_0+80$  s; (d) and (i) at  $t_0+160$  s; (e) and (j) at  $t_0+464$  s (scale bar: 300  $\mu\text{m}$ ).

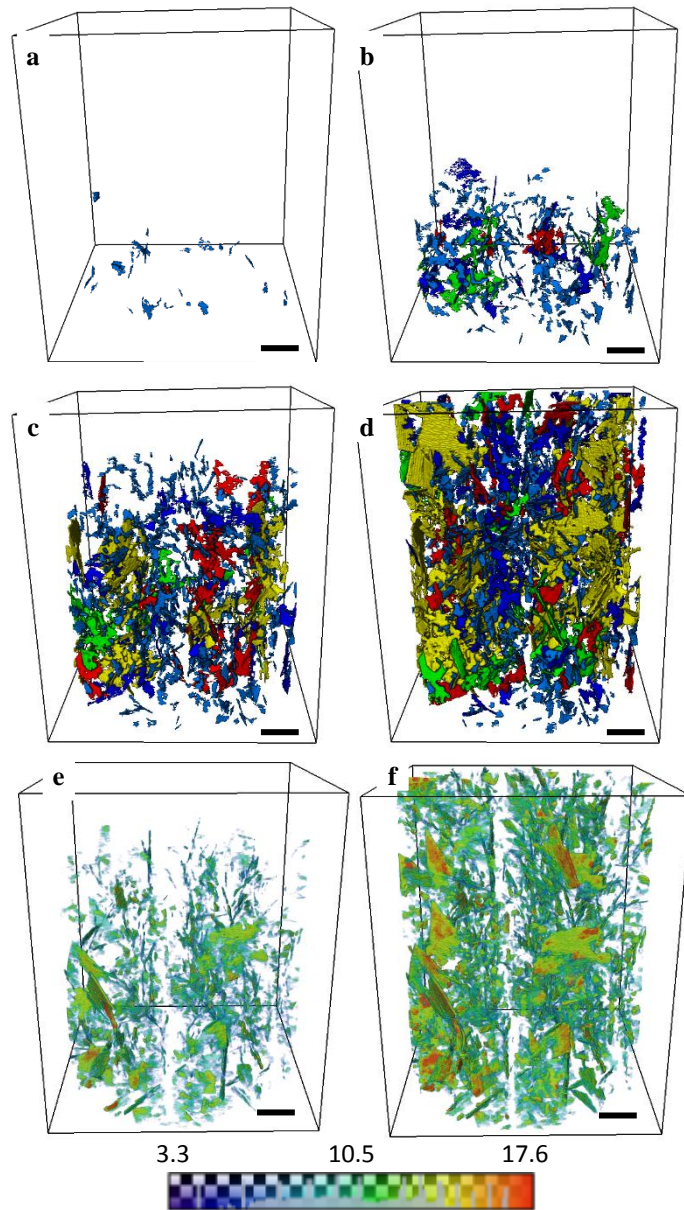


Fig.2. (a) to (d) volume rendering of  $\beta$  intermetallics, at  $t = t_0 +$  (a) 224 s; (b) 288 s; (c) 352 s; and (d) 464 s; (e) and (f) the distribution of local thickness of the  $\beta$  intermetallics at (e) 352 s; and (f) 464 s. (scale bar: 300  $\mu\text{m}$ ).

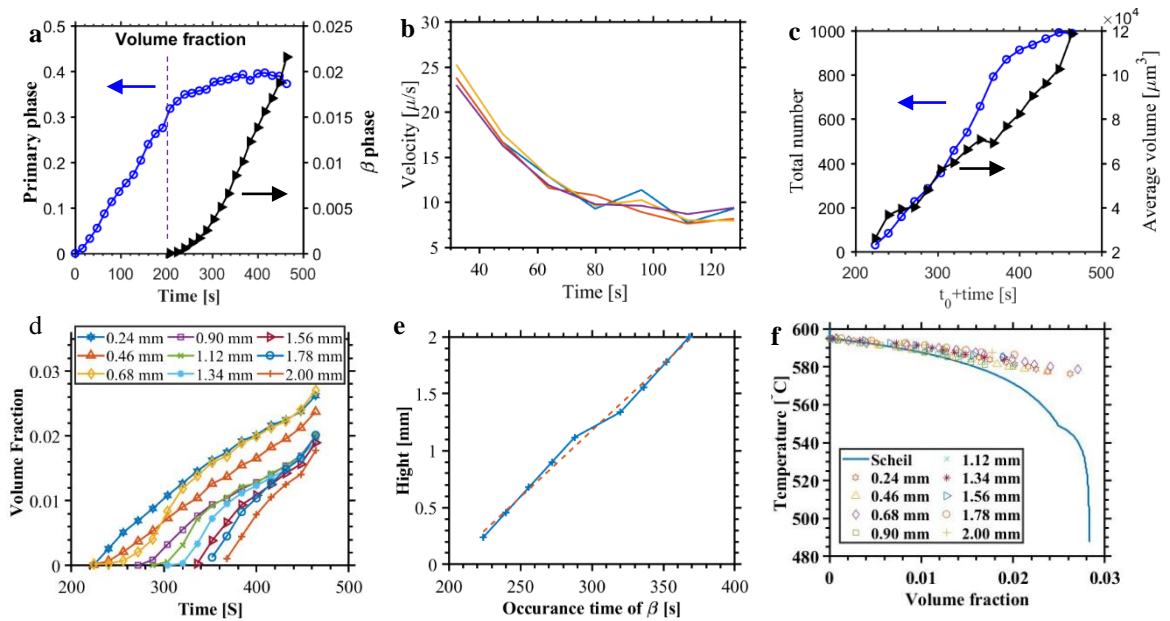


Fig.3. Quantification of the primary and  $\beta$  phase: (a) volume fraction of primary and  $\beta$  phase; (b) the velocity of primary dendrite arm growth; (c) total number and average volume of  $\beta$  particles; (d) volume fraction of  $\beta$  phase at different height of the sample; (e) the first observation of  $\beta$  phase at different heights; and (f) volume fraction of  $\beta$  phase as a function of temperature calculated by Scheil model and tomographic analysis.

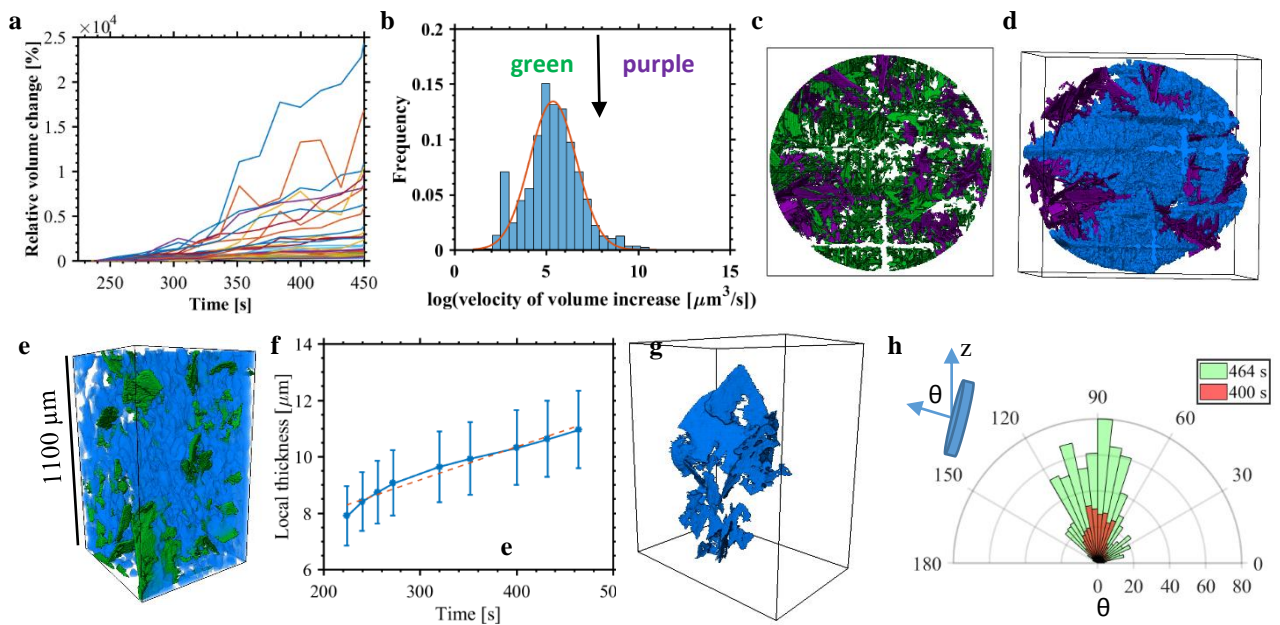


Fig.4. Quantification of individual  $\beta$  intermetallics: (a) the volume change of individual particles appearing from  $t=t_0+240$  s; (b) the histogram of the volume velocity of  $\beta$  particles on a log x-axis; (c)  $\beta$  particles in 3D at  $t=t_0+464$  s color-coded by their velocity (low velocity - green  $< 7000 \mu\text{m}^3/\text{s}$ , high velocity - purple  $> 7000 \mu\text{m}^3/\text{s}$ ); (d)  $\beta$  particles (purple) with high velocity at  $t=t_0+464$  s and the primary phase (blue) at  $t=t_0+128$  s; (e) a region of interests showing  $\beta$  particles with low velocity (green) and primary phase (blue) at  $t=t_0+464$  s; (f) the average local thickness vs time; (g) a connected  $\beta$  particle; and (h) rose histogram of  $\theta$  - angle between the 3rd component of principle component analysis and the vertical direction (Z) of the tomographic volume.

**Supplementary Material**

[Click here to download Supplementary Material: Supplementary.docx](#)